Critical heat flux enhancement model based receding behavior of wicked liquid on nanostructured surfaces

Hong Hyun Son[1], Namgook Kim[1], Sung Joong Kim[1,2*]
[1]*Department of Nuclear Engineering, Hanyang University*
[2]*Institute of Nano Science & Technology, Hanyang University*
222 Wangsimri-ro, Seongdong-gu, Seoul 04763, Republic of Korea
hhson@hanyang.ac.kr, ngkim@hanyang.ac.kr,
[*]*Corresponding author: sungjkim@hanyang.ac.kr*

1. Introduction

Observation of dynamic and thermal activities of dry spots have improved the understanding on mechanism of critical heat flux (CHF) triggering [1]. This study has highlighted that CHF triggers when residual dry spots become an irreversible large dry patch due to relatively lower wetting capacity in hindering the growth of dry area. Based on the successive observation, it has been found that liquid wicking into microlayer effectively delays the growth of residual dry area and increases triple contact line density, of which processes result in CHF enhancement.

However, there is still lack of understanding on receding behavior of wicked liquid along triple contact line because it is difficult to visualize the wicked area around the dry spot due to interference of neighboring vapor bubbles and very short life time ($<10^2$ ms) of reversible dry spots. Moreover, Conventional wetting or wicking experiments (i.e. goniometer and capillary tube) in an attempt to indirectly measure wetting capability have observed wetting or wicking behaviors of liquid without external forces. Thus, these experiments have remained a limit in simulating the receding behavior of the wicked liquid around expanding dry spots.

In this study, we have quantified the receding velocity of the wicked liquid by introducing a new wicking experiment called air-induced wicking experiment. Moreover, CHF enhancement on nanostructures varying with pore size was modelled in light of microlayer dryout mechanism resulting from complete evaporation of the receding wicked liquid volume.

2. Experimental

2.1 Air-induced wicking experiment

The air-induced wicking experiment has been designed to readily observe the wicked liquid around the dry area and its receding behavior varying with structural wicking potential. Figure 1 shows the experimental design. In this experiment, the air compressor puts pressure (0.8 MPa) on a liquid layer remaining on a test sample. Then, air pressure supplied through a metal needle (0.52 mm in inner diameter) makes a dry hole on the target area, and subsequently, recedes circumjacent liquid over lateral direction.

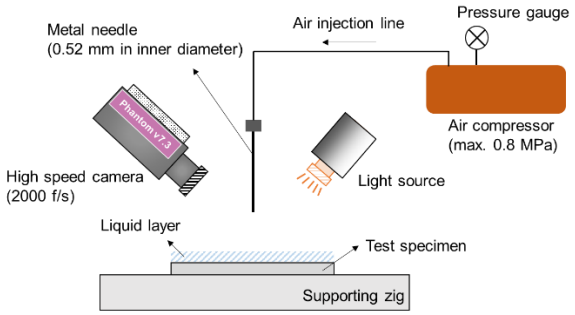

Fig. 1. Design of air-induced wicking experiment.

Figure 2 shows typical liquid receding trend of bare and wick structure surfaces. We found that the wick structure surface makes a wicking front along triple contact line and resists to the growth of dry area while bare surface only makes a wetting front without any wicked liquid area. This observation clearly indicates that the existence of wicked liquid area further delays surface dryout.

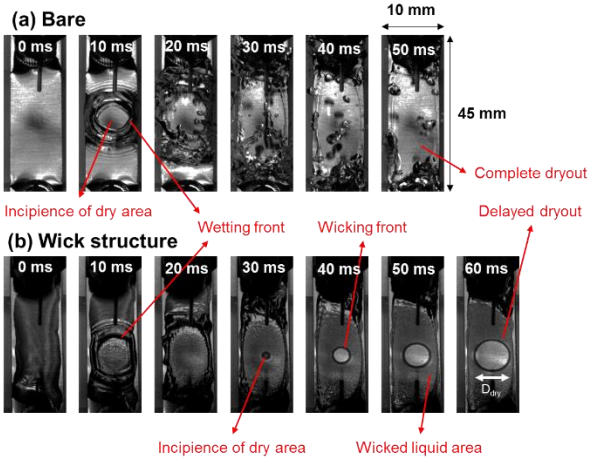

Fig. 2. Observation of receding behavior of wicked liquid on a wick structure. Here, the wick structure is representative as Cr nanostructures.

We believe that this receding behavior of wicked liquid is strongly analogous to the growth mechanism of irreversible dry spots on wick structures. In hydrodynamic analogy (Fig. 3), dry area, wicked area, and wetting front can be substituted for a dry spot, wicked liquid in microlayer, and apparent bubble edge, respectively. Instead of nucleation pressure, air pressure

plays a role in receding wicked liquid front from the incipience of dry area.

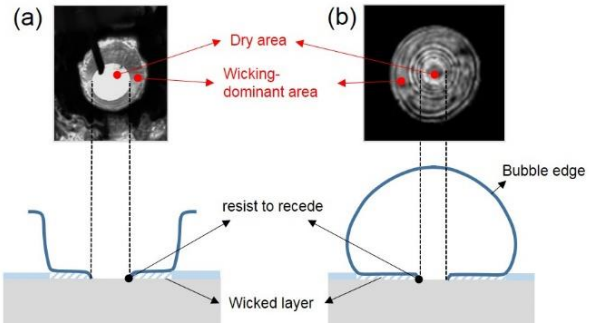

Fig. 3. Hydrodynamic analogy of wicking behavior originated from (a) air pressure and (b) nucleation pressure [2].

We measured the dry diameter D_{dry} with time t and quantified the receding velocity of the wicked liquid by calculating dD_{dry}/dt during 10 ms from the incipience of dry area. The result is discussed in Section 3.1.

2.2 Nanostructure fabrication

To fabricate wick structures in nanoscale, Cr particles were deposited onto a SS304 metal surface using a DC magnetron sputtering. In sputtering process, vacuum pressure and exposure time were 10 mTorr and 1 hr, respectively. Test case was only different with substrate temperature, which set to 25, 150, 300, and 600 °C.

Figure 4 shows Cr nanostructures for different substrate temperatures. Cr particle was shaped as octahedron for all cases. However, particle size decreased with an increase of the substrate temperature. It is possible because for DC sputtering higher substrate temperature induces more active diffusion process, which results in the formation of fine agglomeration. Figure 5 shows the decreasing trend of particle size with substrate temperature.

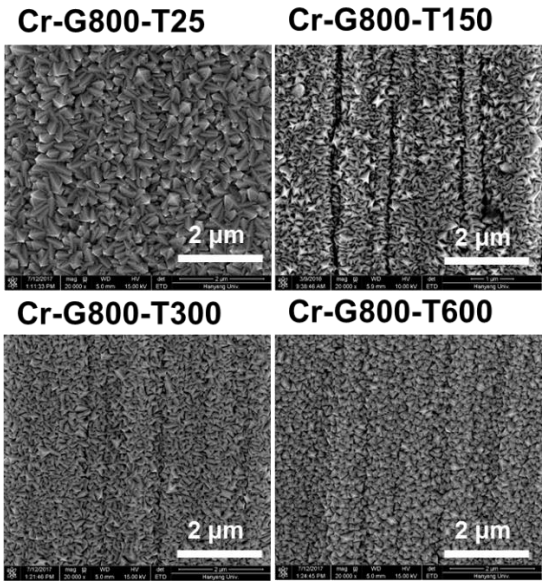

Fig. 4. SEM images of Cr nanostructures after DC magnetron sputtering. (Magnification 20,000 x)

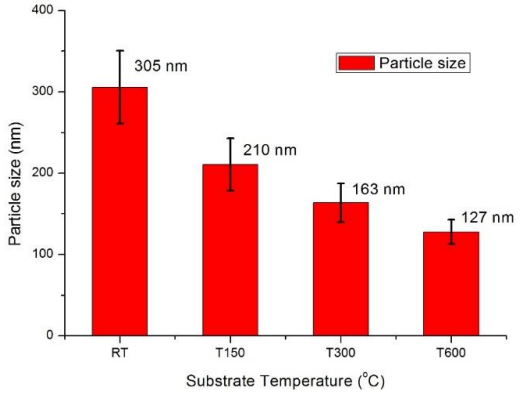

Fig. 5. Decreasing trend of particle size with substrate temperature.

2.3 Pool boiling experiment

The pool boiling chamber was operated with a saturated DI water (18.5 MΩ-cm) at atmospheric pressure. The details of pool boiling apparatus were described in [3].

Figure 6 shows the design of the test section. The test sample is prepared as a flat plate with 45 mm in length (25 mm in heated length), 10 mm in width, and 2 mm in thickness. Here, the width of the test sample is lower than 15.7 mm Taylor wavelength of the saturated water, which indicates only one-dimensional Taylor wavelength along heated length was simulated in this experiment. Thus, it should be noted that this experiment only focuses on the relative comparison of CHF enhancement rather than presenting absolute CHF values.

Joule heating method was adopted to apply steady-state heat flux. A K-type thermocouple was attached to the bottom of the test sample. The side and the bottom of the test sample were covered with high temperature epoxy for thermal and electrical insulations.

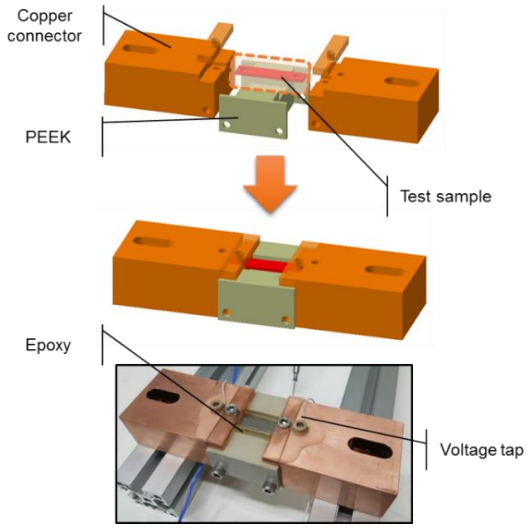

Fig. 6. Design of test section.

Applied heat flux was calculated using a simple heat flux equation as shown in Eq. (1).

$$q'' = \frac{Power}{A_{heated}} = \frac{VI}{LW} \quad (1)$$

V is the voltage drop across the length of the heater, I is the current, L is the heated length, and W is the heated width. Using a propagation of error method, measurement uncertainty was estimated as 4.5%.

3. Result and discussion

Typical microlayer dryout models assume complete evaporation of absorbed liquid in micro/nanostructures. Observations of dynamic behavior of dry spot and liquid microlayer using IR camera have revealed that the wicked liquid recedes from nucleation sits due to the expansion of dry spot and irreversible dry patches occur when the receding wicked liquid volume is completely evaporated.

Thus, in a dynamic point of view, we have focused on the receding behavior of wicked (absorbed) liquid and its complete evaporation. Figure 7 shows a proposed concept. In this concept, for CHF enhancement, microlayer dryout should be delayed when the additional heat capacity in microlayer is supplied with higher resistance to recede (higher capillarity) and/or larger amount of wicked liquid volume (larger particle size or higher surface area ratio). Modeling details are described in light of receding velocity, wicked liquid volume, and critical heat flux.

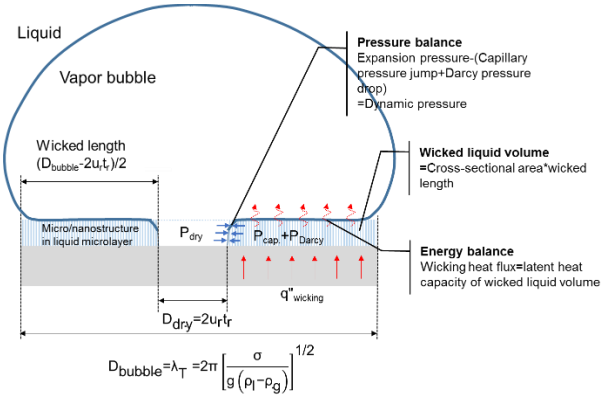

Fig. 7. Schematic of model concept.

3.1 Receding velocity

Considering the receding behavior of the wicked liquid shown in Fig. 2, the dynamic pressure needed to recede is balanced with air pressure P_a, capillary pressure $P_c = \frac{2\sigma cos\theta}{R_p}$, and Darcy frictional pressure $P_D = \frac{\mu L}{\kappa} u_r$. Here, pore size was assumed to be same with particle size. Among involving pressures, the air pressure is a driving pressure while capillary and Darcy frictional pressures are resistant factors to recede. This pressure balance was similarly considered in [4, 5], although they did not reflect the external pressure to simulate the receding behavior of the wicked liquid. Balanced form can be expressed as

$$P_a - \left(\frac{2\sigma cos\theta}{R_p} + \frac{\mu D_{i,dry}}{\kappa} u_r\right) = \frac{1}{2}\rho_l u_r^2 \quad (2)$$

where σ is the surface tension, θ is the intrinsic contact angle, r_p is the pore radius, μ is the liquid viscosity, $D_{i,dry}$ is the diameter of dry area, κ is the permeability, ρ_l is the liquid density, and u_r is the receding velocity. This equation is a quadratic form varying with the receding velocity u_r, which is arranged as

$$u_r = \frac{-\frac{\mu}{\kappa}D_{i,dry} + \sqrt{\left(\frac{\mu}{\kappa}D_{i,dry}\right)^2 + 2\rho_l(P_{dry} - P_c)}}{\rho_l} \quad (3)$$

If the permeability is assumed to be a constant 5.5×10^{-13} m^2 for all cases, which means no pore size dependency, the trend of Eq. (3) is shown as Fig. 8. The receding velocity increases with particle size and air pressure. The receding velocity of Cr nanostructures was ranged from 0.21-0.23 m/s. This result is similar with Eq. (3), although the slight decreasing trend with particle size is hardly matched. We believe that the discrepancy comes from the permeability modeling. For more accurate prediction, particle size should be incorporated into the permeability κ.

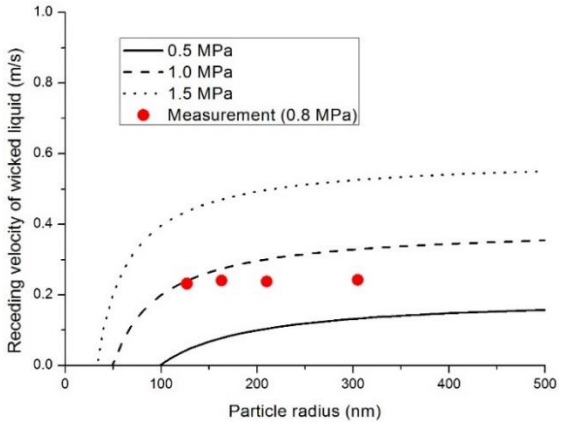

Fig. 8. Comparison between Eq. (1) and measurement.

3.2 Wicked liquid volume

The wicked liquid volume can be expressed with pore volume $\frac{4}{3}\pi R_p^3 sin\theta$, number of pore along contact line $\frac{\pi D}{2R_p}$, and number of pore along receding direction $\frac{dD}{2R_p}$.

To determine remaining wicked liquid length, we assumed that the wicked liquid recedes from a dry spot for the receding time t_r, 15 ms in this calculation, and the diameter of dry spot can be expressed as $2u_rt_r$. Then, the wicked liquid volume on nanostructure exists from $2u_rt_r$ to bubble base diameter D_{bubble}, which is assumed to be same with Taylor wavelength $2\pi\left[\frac{\sigma}{g(\rho_l-\rho_g)}\right]^{1/2}$.

By integrating above expressions, the receding wicked liquid volume can be estimated as

$$V_r = \int_{2u_r t_r}^{D_{bubble}} \frac{4}{3}\pi R_p^3 sin\theta \frac{\pi D}{2R_p}\frac{dD}{2R_p} = \frac{\pi^2}{6} r_p sin\theta [D_{bubble}^2 - (2u_r t_r)^2] \quad (4)$$

Here, the intrinsic contact angle θ of pure Cr was given as 70°, which measured on a pure Cr (3N5) target surface.

3.3 Critical heat flux

When assuming liquid and vapor temperatures are the same with the saturation temperature, the phase change heat capacity of the wicked liquid volume rate $\rho_l h_{fg} Q_l$ can be completely evaporated for the receding time t_r. By limiting the heating area into the bubble base area, wicking heat flux needed to resolve the wicked liquid volume is expressed as

$$q"_{wicking} = C_p \frac{\rho_l h_{fg} Q_l}{A_b} \quad (5)$$

Incorporating Eq. (4) into Eq. (5), the wicking heat flux becomes

$$q"_{wicking} = C_p \frac{2\pi}{3} \rho_l h_{fg} \frac{R_p sin\theta [D_{bubble}^2 - (2u_r t_r)^2]}{D_{bubble}^2 t_r} \quad (6)$$

In Eq. (6), the wicking heat flux mainly depends on pore radius R_p. The typical trend of Eq. (6) is shown as a black line in Fig. 9. The trend is well matched with the measured data with the proportional constant C_p of 5.

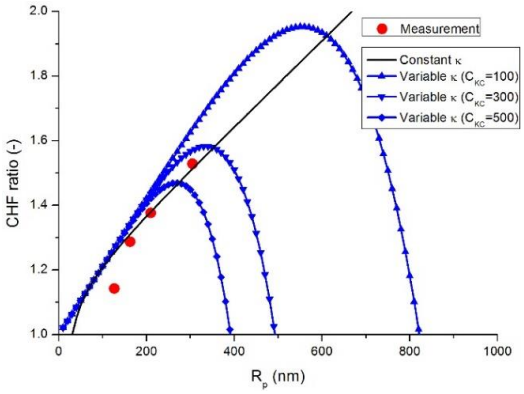

Fig. 9. Prediction of CHF enhancement ratio (red point) with constant (black line) and variable permeabilities (blue line).

However, those monotonic CHF increase seems controversial because we considered Darcy frictional pressure drop in modeling the receding velocity. Although the larger pore size increases the wicked liquid volume, it whereas decreases Darcy frictional pressure drop, which means the reduction of the resistance to recede from the dry spot.

We found that this controversial comes from impractical assumption for constant permeability. Considering variable permeability $\kappa = C_{KC} \frac{R_p^2 \epsilon^3}{(1-\epsilon)^2}$, which depends on pore size, non-monotonic CHF increases (blue lines) were found with different Kozeny-Carman constants C_{KC}. As a future work, more CHF data are needed to predict a sudden decrease region.

4. Conclusions

We introduced the air-induced wicking and successively observed and quantified the receding behavior of the wicked liquid on Cr nanostructures while there is no wicked liquid area on the bare surface. This hydrodynamic analogy supports recent findings that higher liquid area fraction and higher triple contact line density on nanostructures delay the occurrence of irreversible dry spots.

We are developing a CHF enhancement model based on the receding velocity of the wicked liquid. Comparison between CHF data and current model remained some rooms for complete understanding due to insufficiency of permeability modeling. To establish non-monotonic trend, more CHF data varying with particle size in nanoscale are needed near the future.

ACKNOWLEDGEMENT

This research was supported by the Basic Science Research Program through the National Research Foundation of Korea (NRF) funded by the Ministry of Science, ICT & Future Planning (No. NRF-2015R1C1A1A01054861), and by the National Research Foundation of Korea (NRF) grant funded by the Korean government (MSIP: Ministry of Science, ICT and Future Planning) (No. NRF-2017M2A8A5018575)

REFERENCES

[1] D.E. Kim, J. Song, and H. Kim, Simultaneous observation of dynamics and thermal evolution of irreversible dry spot at critical heat flux in pool boiling, International Journal of Heat and Mass Transfer, Vol. 99, pp. 409-424, 2016.

[2] S. Jung and H. Kim, An Experimental Study on Heat Transfer Mechanisms in the Microlayer using Integrated Total Reflection, Laser Interferometry and Infrared Thermometry Technique, Heat Transfer Engineering, Vol. 36, No. 12, 1002-1012, 2015.

[3] H.H. Son, G.H. Seo, U. Jeong, D.Y. Shin, and S.J. Kim, Capillary wicking effect of a Cr-sputtered superhydrophilic surface on enhancement of pool boiling critical heat flux, International Journal of Heat and Mass Transfer, Vol. 113, pp. 115-128, 2017,.

[4] M. Tetreault-Friend, R. Azizian, M. Bucci, T. McKrell, J. Buongiorno, M. Rubner and R. Cohen, Critical heat flux maxima resulting from the controlled morphology of nanoporous hydrophilic surface layers, Applied Physics Letters, Vol. 108, No. 24, p. 243102, 2016.

[5] S.H. Kim, G.C. Lee, J.Y. Kang, K. Moriyama, M.H. Kim and H.S. Park, Boiling heat transfer and critical heat flux evaluation of the pool boiling on micro structured surface, International Journal of Heat and Mass Transfer, Vol. 91, pp. 1140-1147, 2015.